Electronic Supplementary Material (ESI) for Energy & Environmental Science.

Supplementary information for:

High performance Li-, Na-, and K-ion storage in electrically conducting coordination polymers

Jiande Wang,† Xiaolong Guo,† Petru Apostol,† Xuelian Liu,† Koen Robeyns,† Loïk Gence,§ Christian Morari,‡ Jean-François Gohy,† and Alexandru Vlad†*

† Institute of Condensed Matter and Nanosciences, Université catholique de Louvain, Louvain-la-Neuve, Belgium

‡ Institutul Național de Cercetare-Dezvoltare pentru Tehnologii Izotopice și Moleculare Cluj-Napoca, Cluj-Napoca, România

§ Instituto de Física, Pontificia Universidad Católica de Chile, Santiago, Chile

**E-mail: alexandru.vlad@uclouvain.be*

Table of Contents

Materials and synthesis

1.1 Materials

1,2,4,5-Benzenetetramine tetrahydrochloride (Fluorochem), pyridine (Fisher Scientific), methanesulfonyl chloride (Acros Organics), lithium methoxide (TCI Europe), sodium methoxide (TCI Europe), potassium methoxide (TCI Europe), anhydrous methanol (Alfa Aesar), anhydrous diethyl ether (Alfa Aesar), anhydrous cobalt (II) chloride (Alfa Aesar), anhydrous iron (II) chloride (Alfa Aesar), anhydrous manganese (II) chloride (Sigma Aldrich) were used as received.

1.2 Synthesis of H_4-PTtSA

To a solution of 1,2,4,5-Benzenetetramine tetrahydrochloride (2.48 g, 0.01 mol, Fluorochem) in 50 ml pyridine, methanesulfonyl chloride (3.25 ml, 42 mmol, Acros organics) was added drop-wise for a duration of 30 minutes at 0 °C. The solution was left to warm up slowly to room temperature and was kept stirring for another 24 h. After, 200 ml of 1 M HCl solution was added to the solution and the precipitate was washed with a large amount of 1 M HCl solution and water to obtain the H_4-PTtSA solid. The final product was dried under vacuum at 70 °C.

1.3 Synthesis of Li_2-Co-PTtSA

A solution of Li_4-PTtSA was prepared by mixing H_4-PTtSA (225 mg, 0.5 mmol) and lithium methoxide (76 mg, 2 mmol) in anhydrous methanol (5 ml) under inert atmosphere. Another solution of $CoCl_2$ was prepared by dissolving anhydrous cobalt (II) chloride (65 mg, 0.5 mmol) in anhydrous methanol (3 ml). The two solutions were mixed and kept stirring for 48 h under inert atmosphere. The obtained precipitate was filtered and washed with methanol and diethyl ether. The obtained solid was dried at 60 °C for 2 h, followed by drying at 180 °C for 4 h.

1.4 Synthesis of Li_2-Fe-PTtSA

A solution of Li_4-PTtSA was prepared by mixing H_4-PTtSA (225 mg, 0.5 mmol) and lithium methoxide (76 mg, 2 mmol) in anhydrous methanol (5 ml) under inert atmosphere. Another solution of $FeCl_2$ was prepared by dissolving anhydrous iron (II) chloride (63.4 mg, 0.5 mmol) in anhydrous methanol (3 ml). The two solutions were mixed and kept stirring for 48 h under inert atmosphere. The obtained precipitate was filtered and washed with methanol and diethyl ether. The obtained solid was dried at 60 °C for 2 h, followed by drying at 180 °C for 4 h.

1.5 Synthesis of Li_2-Mn-PTtSA

A solution of Li_4-PTtSA was prepared by mixing H_4-PTtSA (225 mg, 0.5 mmol) and lithium methoxide

(76 mg, 2 mmol) in anhydrous methanol (5 ml) under inert atmosphere. Another solution of $MnCl_2$ was prepared by dissolving anhydrous manganese (II) chloride (62.9 mg, 0.5 mmol) in anhydrous methanol (3 ml). The two solutions were mixed and kept stirring for 48 h under inert atmosphere. The precipitate was filtered and washed with methanol and diethyl ether. The obtained solid was dried at 60 °C for 2 h, followed by drying at 180 °C for 4 h.

1.6 Synthesis of Na_2-Co-PTtSA

A solution of Na_4-PTtSA was prepared by mixing H_4-PTtSA (225 mg, 0.5 mmol) and sodium methoxide (108 mg, 2 mmol) in anhydrous methanol (5 ml) under inert atmosphere. Another solution of $CoCl_2$ was prepared by dissolving anhydrous cobalt (II) chloride (65 mg, 0.5 mmol) in anhydrous methanol (3 ml). The two solutions were mixed and kept stirring for 48 h under inert atmosphere. The precipitate was filtered and washed with methanol and diethyl ether. The obtained solid was dried at 60 °C for 2 h, followed by drying at 180 °C for 4 h.

1.7 Synthesis of K_2-Co-PTtSA

A suspension of K_4-PTtSA was prepared by mixing H_4-PTtSA (225 mg, 0.5 mmol) and potassium methoxide (140 mg, 2 mmol) in anhydrous methanol (5 ml) under inert atmosphere. Another solution of $CoCl_2$ was prepared by dissolving anhydrous cobalt (II) chloride (65 mg, 0.5 mmol) in anhydrous methanol (3 ml). The two solutions were mixed and kept stirring for 48 h under inert atmosphere. The precipitate was filtered and washed with methanol and diethyl ether. The obtained solid was dried at 60 °C for 2 h, followed by drying at 180 °C for 4 h.

1.8 Synthesis of Li_2-*o*-Co-PTtSA

A solution of Li_2-*o*-PDSA was prepared by mixing H_2-*o*-PDSA (264 mg, 1 mmol) and lithium methoxide (76 mg, 2 mmol) in anhydrous methanol (5 ml) under inert atmosphere. Another solution of $CoCl_2$ was prepared by dissolving anhydrous cobalt (II) chloride (65 mg, 0.5 mmol) in anhydrous methanol (3 ml). The two solutions were mixed and kept stirring for 48 h under inert atmosphere. Large amount of diethyl ether was added into the reaction, and precipitate was filtered and washed with diethyl ether 3 times. The single crystal of Li_2-*o*-Co-PTtSA was prepared by diffusion of diethyl ether into a solution of Li_2-*o*-Co-PTtSA in methanol.

Materials characterizations

Fourier transform Infra-Red (FTIR) spectroscopy was performed on an Agilent Technologies Cary 630 FTIR operated in ATR mode, measured in the wavenumber range from 4000 cm^{-1} to 650 cm^{-1} at a resolution of 4 cm^{-1} with 64 scans. Powder X-ray powder diffraction (PXRD) patterns were collected on a STOE DARMSTADT StadiP Transmission diffractometer system using Cu Kα1 radiation with a wavelength of 1.54059 Å. Elemental analysis was performed by Medac Ltd, where the CHNS analysis was done by elemental combustion, the F by ion-chromatography and the metals content by ICP-OES. For ex-situ elemental analysis, electrodes were made with 30% of Super P carbon and 70% of active materials.

Electrical conductivity measurements.

Pellets (10 mm in diameter) were prepared by pressing the powder at 384 MPa while keeping the sample under a protective Ar atmosphere. The powder was pressed between two carbon coated aluminum foils to ensure a good electrical contact. The pressed pellets were encapsulated in home-made Swagelok cells (inside an Ar filled Glove box), and transferred to a climatic chamber for variable temperature electrical conductivity measurements. The conductivity measurements were carried out by using Biologic two-probe d.c. current–voltage technique.

Half-cell assembly and testing

The tests were performed in 2032-type coin cells with 13 mm alkali-metal chips (Li, Na, K) as the counter / reference electrodes, and glass microfiber filters (WhatmanGF/D, Aldrich) as the separators. The thickness of the metal chips is around 1 mm, with a diameter of 13-15 mm. The positive electrode composition was prepared by hand-grinding 50 - 90 wt.% of active material with 5 - 40 wt.% conductive carbon Super P and 5 wt.% or 10 wt.% PTFE as binder. The electrodes were prepared by adding the grinded powder onto the positive side of the coin cell case (CR 2032, AISI 316L stainless steel) and pressed with a stainless-steel disk for compaction. Electrode mass loading was varied between 5 and 50 mg/cm^2 for electrochemical evaluation. Galvanostatic charge/discharge tests were performed with Neware battery testing system in a climatized room (nominal of 22 °C, with small and short period variations possible). For Lithium cells, 1 M LiTFSI in PC was used as electrolyte, while 1M NaPF$_6$ EC/DEC and KTFSI: 1-Ethyl-3-methylimidazolium Bis(trifluoromethanesulfonyl)imide (1: 9 molar ratio) were used for Sodium and Potassium cells, respectively. The electrolyte amount is 80 – 100 µL for one coin cell with electrode of 5 mg/cm^2. More electrolyte was generally used for higher mass loaded cells.

Battery testing in low earth orbit (LEO) space environment

Thermal stress cycles were performed as follows: cells were firstly characterized in their as assembled state for 40 cycles at room temperature, and introduced hereafter in the chamber for thermal stress testing. The environment consisted in a homemade vacuum chamber, equipped with a sample holder built with ceramic heater and a thermocouple thermometer. The chamber was pumped down with a turbomolecular pump (Pfeiffer HiCube 80 Eco), monitoring the pressure with a Pfeiffer Vacuum Active Pirani/Cold Cathode Transmitter PKR 251, Full Range, (KF40, PTR2600). A HP Agilent 3245 Precision source and high-resolution multimeter (DMM's) from Keithley were used for cycling tests.

Li_2-Co-PTtSA/graphite full-cell assembly and testing

Glass microfiber filters (WhatmanGF/D, Aldrich) was used as separator, and 1M $LiPF_6$ EC/DMC as electrolyte. The electrodes were prepared by mixing 60% active materials with 30% conductive super P carbon and 10% PTFE by hand grinding. The electrode powder was put into the positive side of the coin cell case and pressed with a stainless-steel disk for compaction. Mass loading for the positive electrodes was around 5 mg/cm^2, with a negative to positive electrode capacity ratio of around 1.5. The graphite anodes were pre-cycled to avoid lithium loss during the SEI formation, and then washed and collected for full-cell assembly. Galvanostatic charge-discharge tests were performed on a Neware battery testing system at 22 °C.

Table S1. Comparative analysis of A_2-TM-PTtSA with previously reported organic alkali-cation reservoir cathodes.

	Positive electrode (or “cathode”) active materials	Negative electrode (or “anode”)	Output voltage (V)	Achieved reversible capacity (mA h g^{-1})	Active material content (%), Mass loading (mg cm^{-2})	Electrode specific Energy (Wh kg^{-1})	Cycling stability: retention, cycles, rate or current density	References
Li-ion cathodes	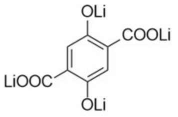	Li-metal	2.45	115 (220)	66, - (65, 2.0)	186 (350)	91.5%, 80, 0.2C (95%, 50, 0.1C)	4 (5)
	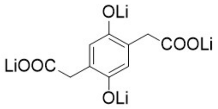	Li-metal	3.35	150	60, 5.0	288	50%, 20, 0.1C	6
	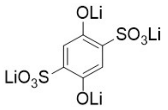	Li-metal	3.15	86	65, -	176	74%, 50, 0.05C	7
	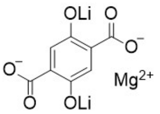	Li-metal	3.35	100	66, -	221	90%, 80, 0.1C	8
	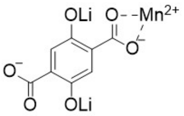	Li-metal	3.2	65	50, 5.0	104	91%, 100, 0.1C	9
	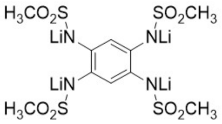	Li-metal	2.75	113	50, 5.0	155	95%, 50, 0.1C	10
	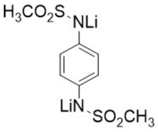	Li-metal	1.4, 3.1	140	50, 5.0	180	80%, 50, 0.1C	10
	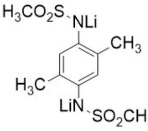	Li-metal	3.0	105	50, 5.0	157	50%, 3, 0.1C	10
	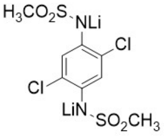	Li-metal	3.25	145	50, 5.0	235	-, -, 0.1C	10
Na-ion cathodes	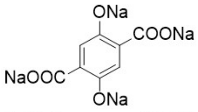	Na-metal	2.4	183	65, 1.8	285	84%, 100, 0.1C	11
	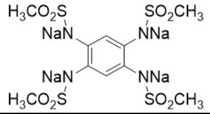	Na-metal	2.5	95	50, 5.0	119	99%, 100, 0.1C	12

K-ion cathode	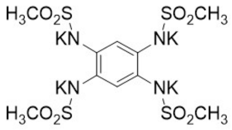	K-metal	2.6	80	50, 5.0	104	50%, 100, 0.1C	12
This work	**Li$_2$-TM-PTtSA (TM = Fe, Co, Mn)**	**Li-metal**	**2.9, 3.5**	**100**	**80, 50**	**256**	**98%, 100, 0.2C (96%, 1000, 5C)**	**This work**
	Na$_2$-Co-PTtSA	**Na-metal**	**2.75, 3.25**	**94**	**80, 5**	**240**	**99%, 100, 0.2C**	**This work**
	K$_4$-Co-PTtSA	**K-metal**	**2.9, 3.55**	**83**	**80, 5**	**215**	**82%, 100, 0.2C**	**This work**

Comment: Table S1 lists the SoA of organic alkali-cation reservoir cathode materials, which are divided into two categories: the conjugated Li-enolates and the conjugated Li-sulfonamides. From this overview it is clear that organic alkali-reservoir cathodes are still in their early stage compared to their inorganic counterparts. First of all, for the previous reported Li-ion reservoir cathodes, they either have a low redox potential (not suitable for cathode application) or require large amount of conductive additives and display unsatisfactory cycling stability. Enhanced capacity retention with cycling can be often seen in the literature, yet many are based on cells with large amount of high surface area carbon (e.g. ketjen black) used, which has a major contribution to the attained capacities. Such data should be considered carefully for comparison to avoid misleading and discarding other's work. Additionally, due to the electrically insulating nature of most organic electrode materials, high carbon content has to be used, resulting in low overall electrode energy with also low high-current performance, which is also the case for the previous reported organic cathodes. Compared to the relatively rich Li-ion cathode family, the reports on Na-ion and K-ion cathodes are scarce, with the few reported still facing a major challenge of low redox potential. On the contrary, the compounds reported in this work all show excellent rate capability, remarkable cycling stability, outstanding tolerance to low carbon content (10 wt.%), high mass loading (50 mg/cm^2), and even extreme utilization conditions. The Na- and K-ion versions of the coordination polymers show an increase of about 500 mV and 700 mV in redox potential compared with the best previously reported Na- and K-reservoir cathodes, respectively. All the coordination polymers in this work show excellent cycling stability with phases insolubility under any charge states, which is also superior to the previous reported small molecule battery materials.

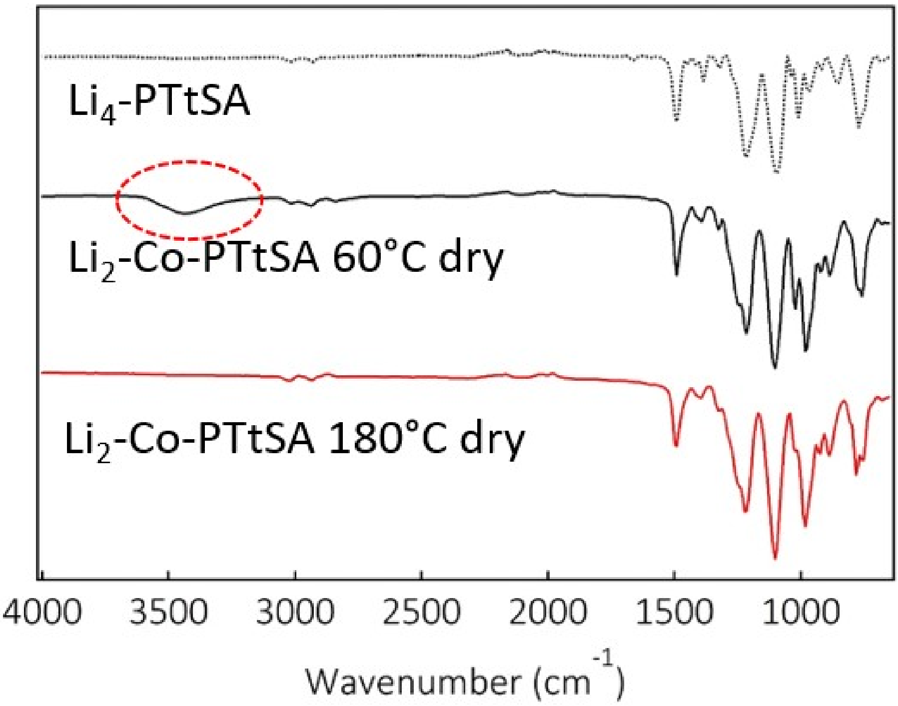

Figure S1. FTIR of Li$_2$-Co-PTtSA before and after desolvation performed at 180 °C under vaccum, and the comparison of FTIR spectra between Li$_2$-Co-PTtSA and Li$_4$-PTtSA. The desolvation was confirmed by the complete disappearance of the broad OH band of methanol located at ~3300 cm^{-1}. Data for Li$_4$-PTtSA data is reproduced with permission from reference [1].

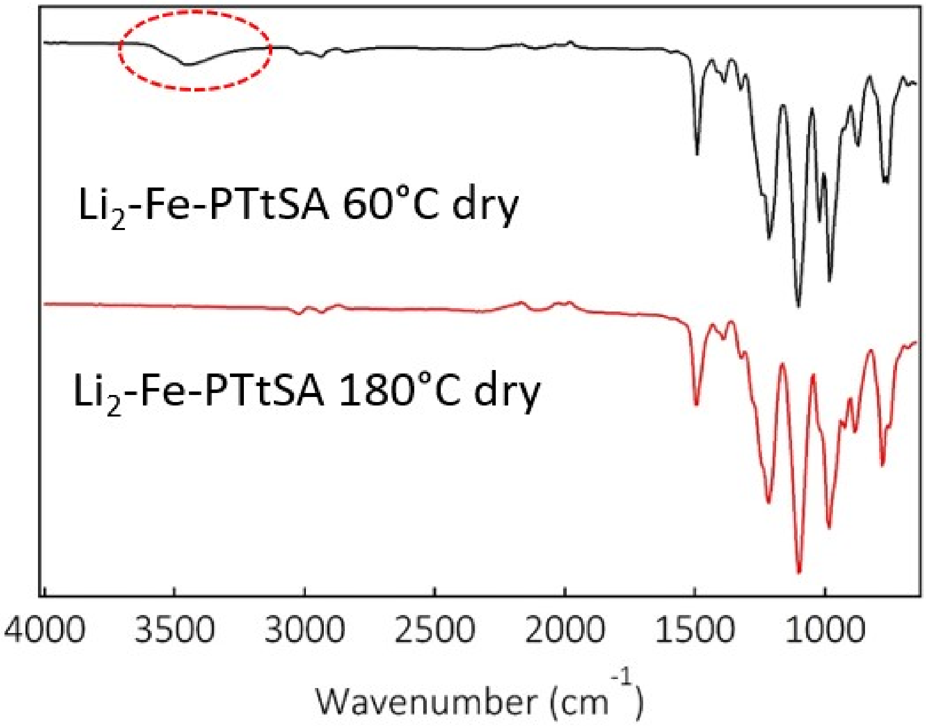

Figure S2. FTIR of Li$_2$-Fe-PTtSA before and after desolvation performed at 180 °C under vacuum. The desolvation was confirmed by the complete disappearance of the broad OH band of methanol located at ~3300 cm^{-1}.

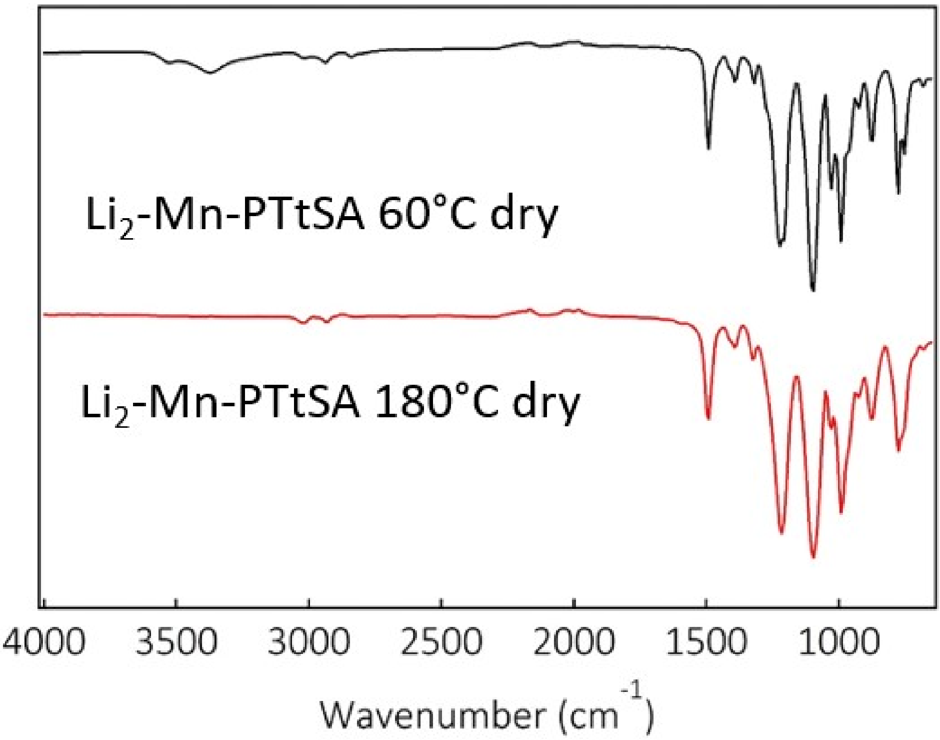

Figure S3. FTIR of Li$_2$-Mn-PTtSA before and after desolvation performed at 180 °C under vacuum. The desolvation was confirmed by the complete disappearance of the broad OH band of methanol located at ~3300 cm^{-1}.

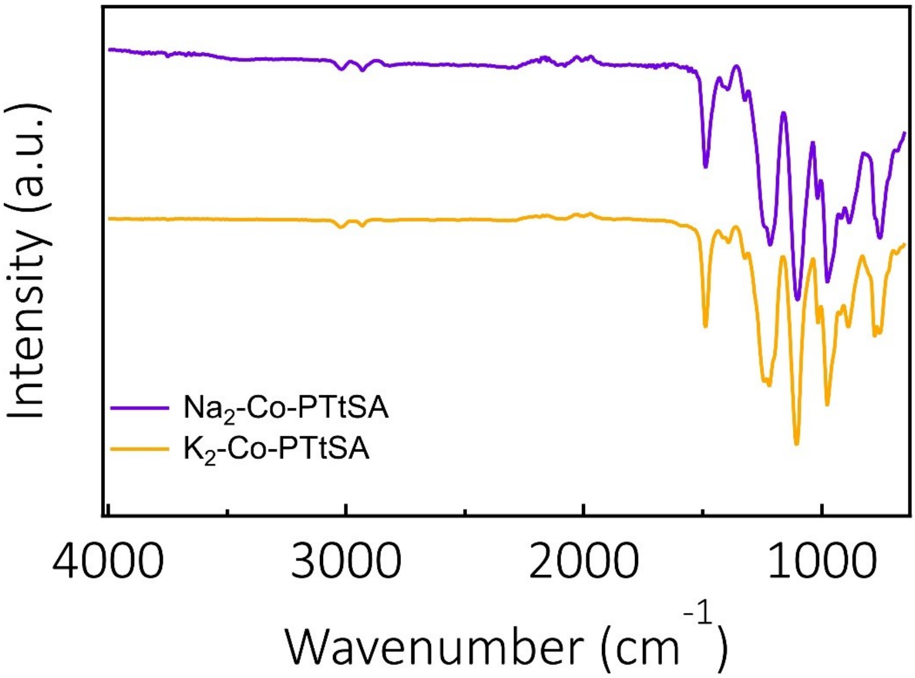

Figure S4. FTIR of Na$_2$-Co-PTtSA and K$_2$-Co-PTtSA after desolvation performed at 180 °C under vacuum.

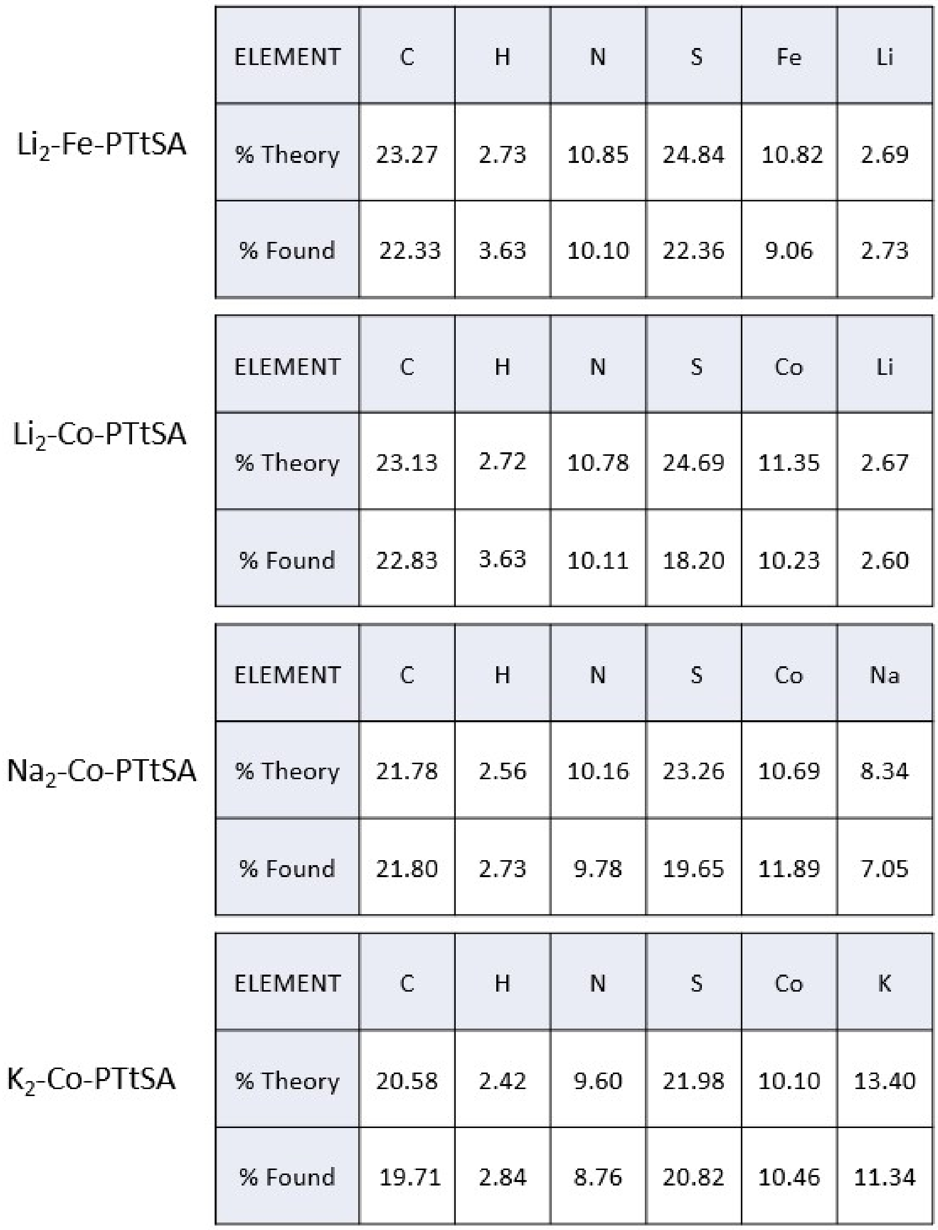

Li_2-Fe-PTtSA

ELEMENT	C	H	N	S	Fe	Li
% Theory	23.27	2.73	10.85	24.84	10.82	2.69
% Found	22.33	3.63	10.10	22.36	9.06	2.73

Li_2-Co-PTtSA

ELEMENT	C	H	N	S	Co	Li
% Theory	23.13	2.72	10.78	24.69	11.35	2.67
% Found	22.83	3.63	10.11	18.20	10.23	2.60

Na_2-Co-PTtSA

ELEMENT	C	H	N	S	Co	Na
% Theory	21.78	2.56	10.16	23.26	10.69	8.34
% Found	21.80	2.73	9.78	19.65	11.89	7.05

K_2-Co-PTtSA

ELEMENT	C	H	N	S	Co	K
% Theory	20.58	2.42	9.60	21.98	10.10	13.40
% Found	19.71	2.84	8.76	20.82	10.46	11.34

Figure S5. Elemental analysis of the pristine A_2-TM-PTtSA coordination polymers obtained by combined CHNSO and ICP-EOS elemental analysis.

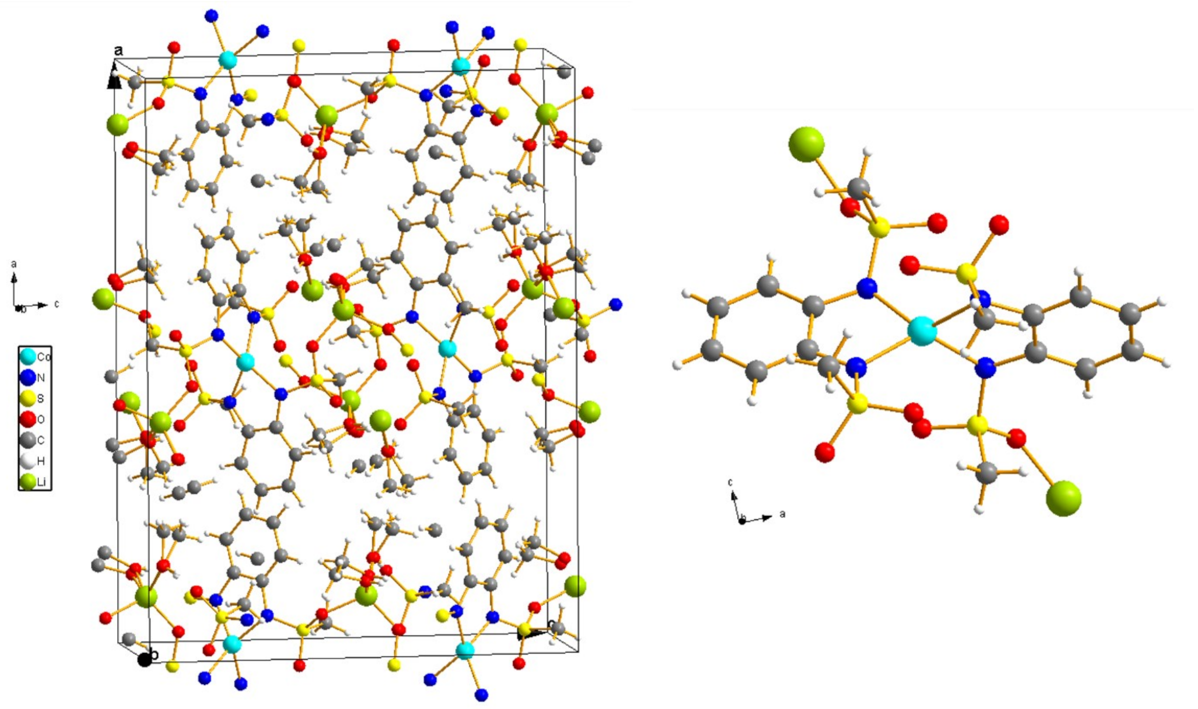

Figure S6. Crystal structure of Li$_2$-*o*-Co-PDSA. The structure shows a distorted tetrahedral coordination environment around the divalent transition metal cation (Co^{2+}) formed by the four N$^-$ centers. The two alkali cations (Li$^+$ in this case) required for charge compensation are coordinated by the oxygen atoms of the -SO$_2$- groups.

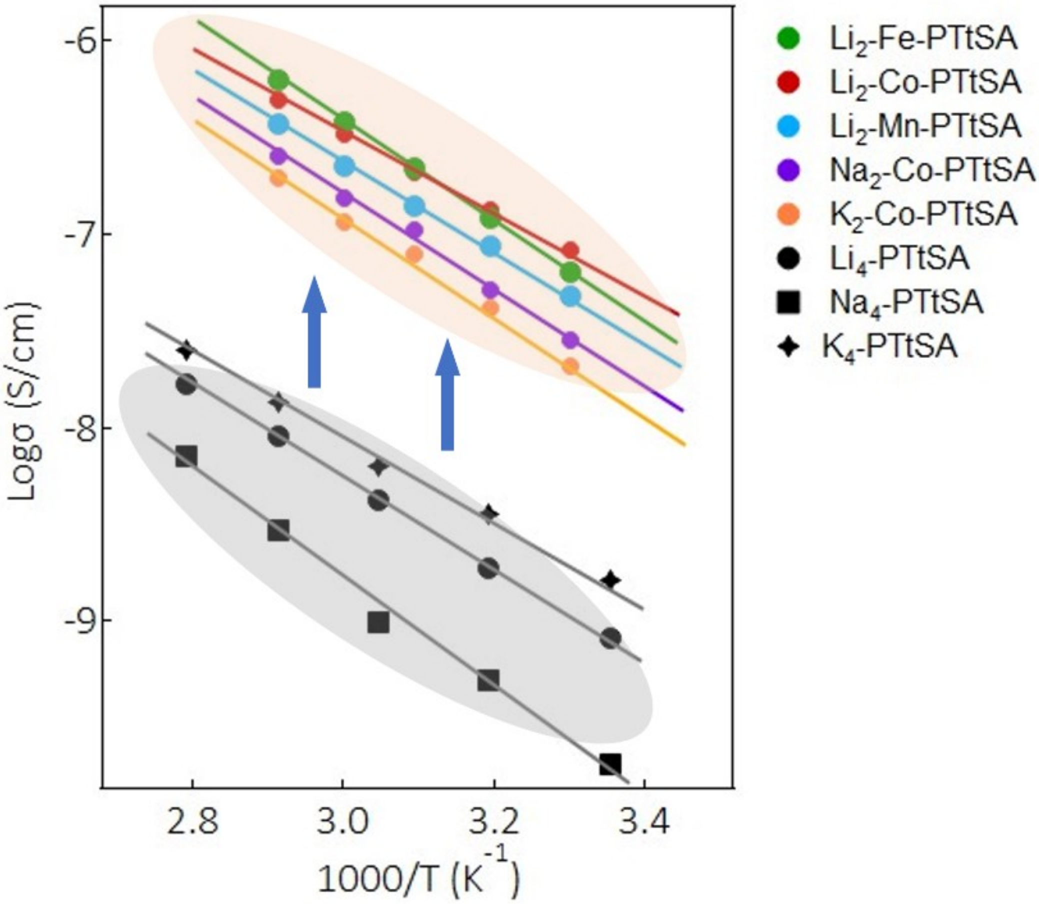

Figure S7. Electrical conductivity of A$_2$-TM-PTtSA (A = Li$^+$, Na$^+$, K$^+$; TM = Fe^{2+}, Co^{2+}, Mn^{2+}) coordination polymers as compared to the alkali-cation analogues A$_4$-PTtSA (A = Li$^+$, Na$^+$, K$^+$). The A$_2$-TM-PTtSA coordination polymers display two orders magnitude conductivity increase. Data for A$_4$-PTtSA series is reproduced with permission from reference [1].

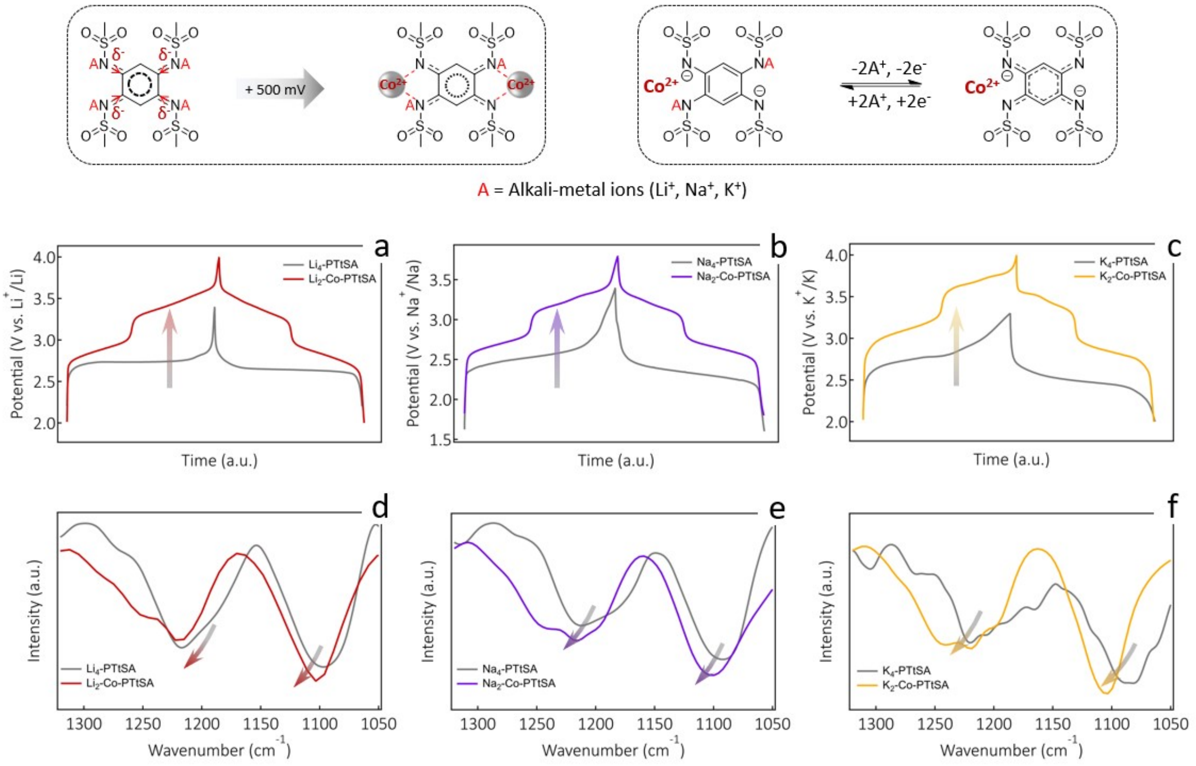

Figure S8. Comparing the properties and performances of A$_2$-Co-PTtSA (A = Li$^+$, Na$^+$, K$^+$) CPs with the alkali-cation analogues A$_4$-PTtSA (A = Li$^+$, Na$^+$, K$^+$). (a), (b) and (c) galvanostatic charge-discharge curves, and the redox potential enhancement effect; (d), (e) and (f) Shift of the vibration frequency of the -SO$_2$- band. Compared to A$_4$-PTtSA analogues, all CPs studied in this work systematically displayed higher redox potential. This is rationalized via the inductive effect of the TM^{2+} cation. The introduction of transition metals also induces redox plateau changes. Whereas only one two-electron plateau process is observed for A$_4$-PTtSA, a sequential two one-electron processes are observed for all A$_2$-TM-PTtSA CPs. A$_4$-PTtSA data is reproduced with permission from reference [1].

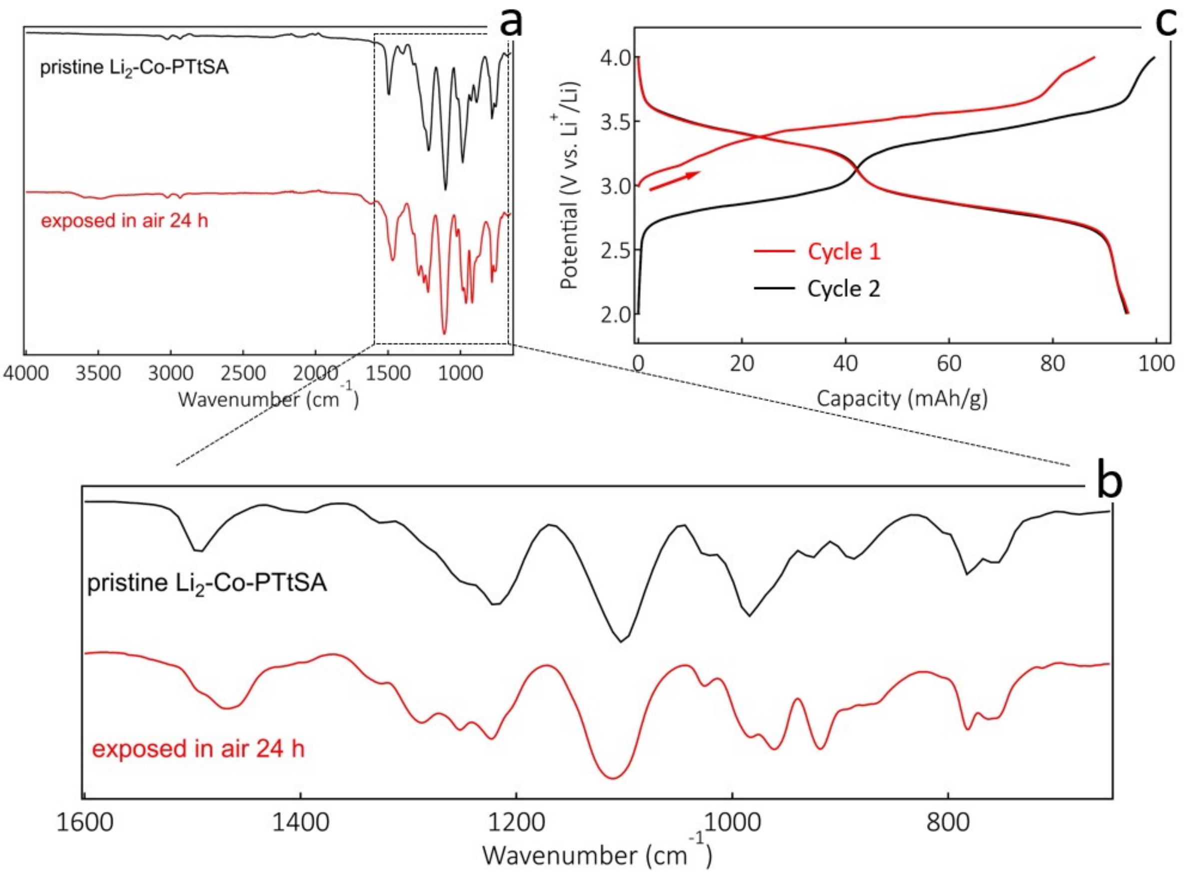

Figure S9. Air stability analysis of Li_2-Co-PTtSA. (a) FTIR comparison of Li_2-Co-PTtSA in pristine state and after exposed to ambient air for 24 hours; (b) FTIR of the zoomed region of (a); (c) The galvanostatic charge-discharge potential vs capacity profile for the air-exposed Li_2-Co-PTtSA. There is only minor oxidation (or hydrolysis) after exposing the sample to air indicated also by the lower 1st cycle charge capacity. No material decomposition is observed, as demonstrated by the excellent capacity retention at the following cycles.

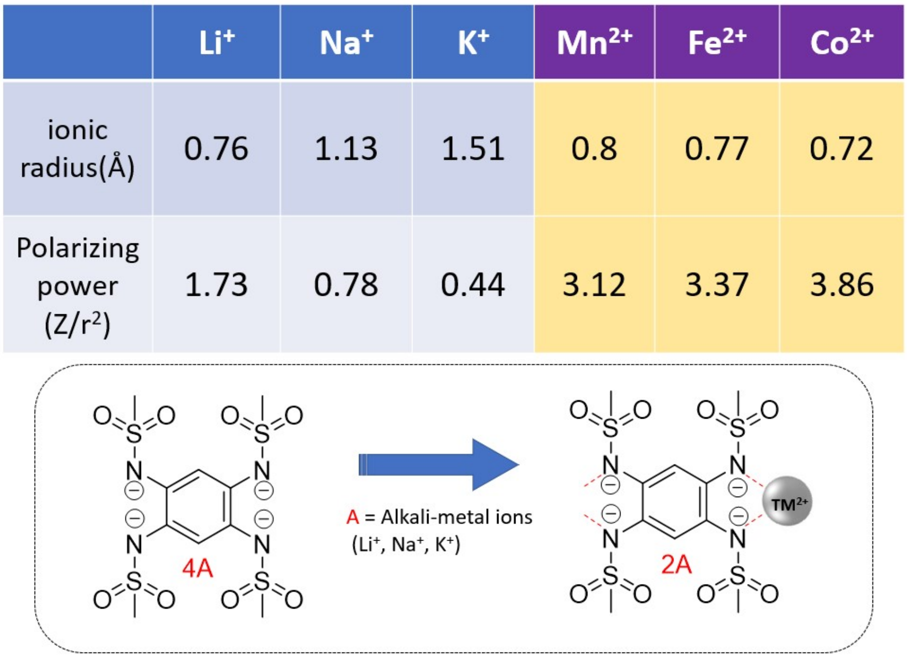

	Li$^+$	Na$^+$	K$^+$	Mn^{2+}	Fe^{2+}	Co^{2+}
ionic radius(Å)	0.76	1.13	1.51	0.8	0.77	0.72
Polarizing power (Z/r^2)	1.73	0.78	0.44	3.12	3.37	3.86

Figure S10. Ionic radius and the polarizing power of selected alkali-cations and divalent transition-metal cations. The used in this work transition metal cations have much higher polarizing power than alkali cations - Co^{2+} has the highest value and Mn^{2+} has the lowest value in the series – correlated with the trend observed for the redox potential enhancement.

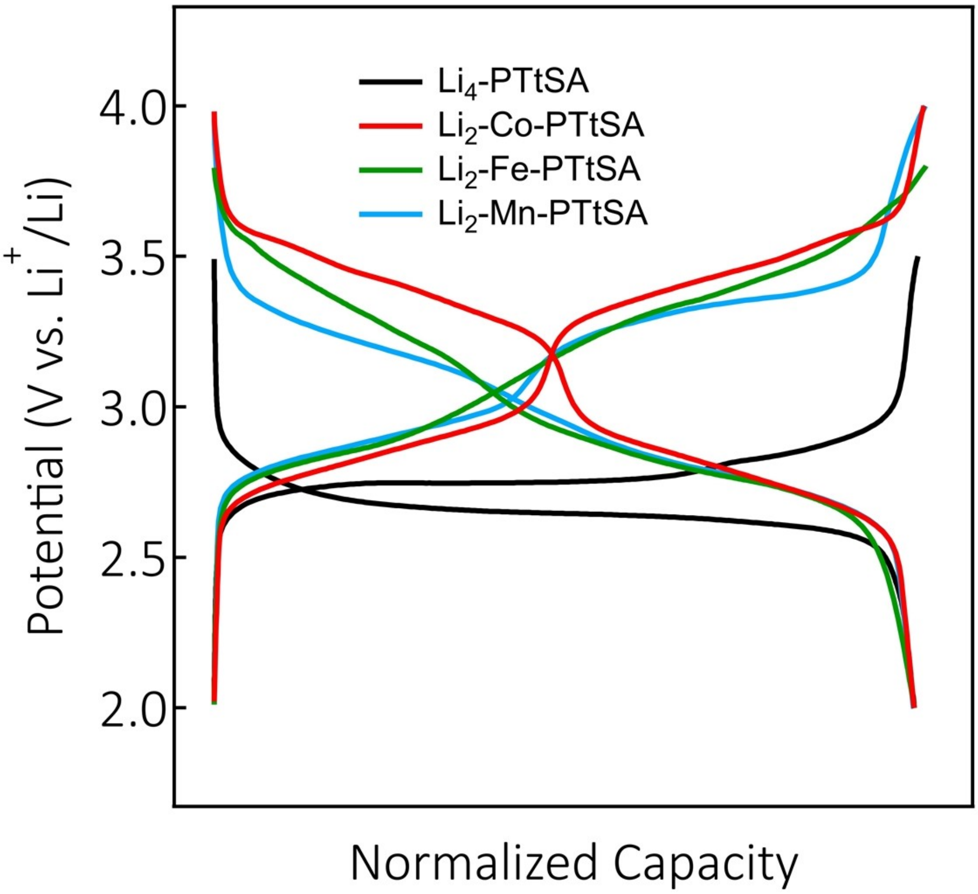

Figure S11. Comparison of the potential vs normalized capacity profiles between Li$_4$-PTtSA and Li$_2$-TM-PTtSA (TM = Co^{2+}, Fe^{2+}, Mn^{2+}). Compared to the average redox potential of 2.75 V vs. Li$^+$/Li for Li$_4$-PTtSA, the Li$_2$-TM-PTtSA shows two separated redox plateaus, at higher potential, averaging above 3 V. Amongst, Li$_2$-Co-PTtSA shows the most distinct separation between the two plateaus, making this composition particularly interesting to investigate the intermediate one-electron redox state.

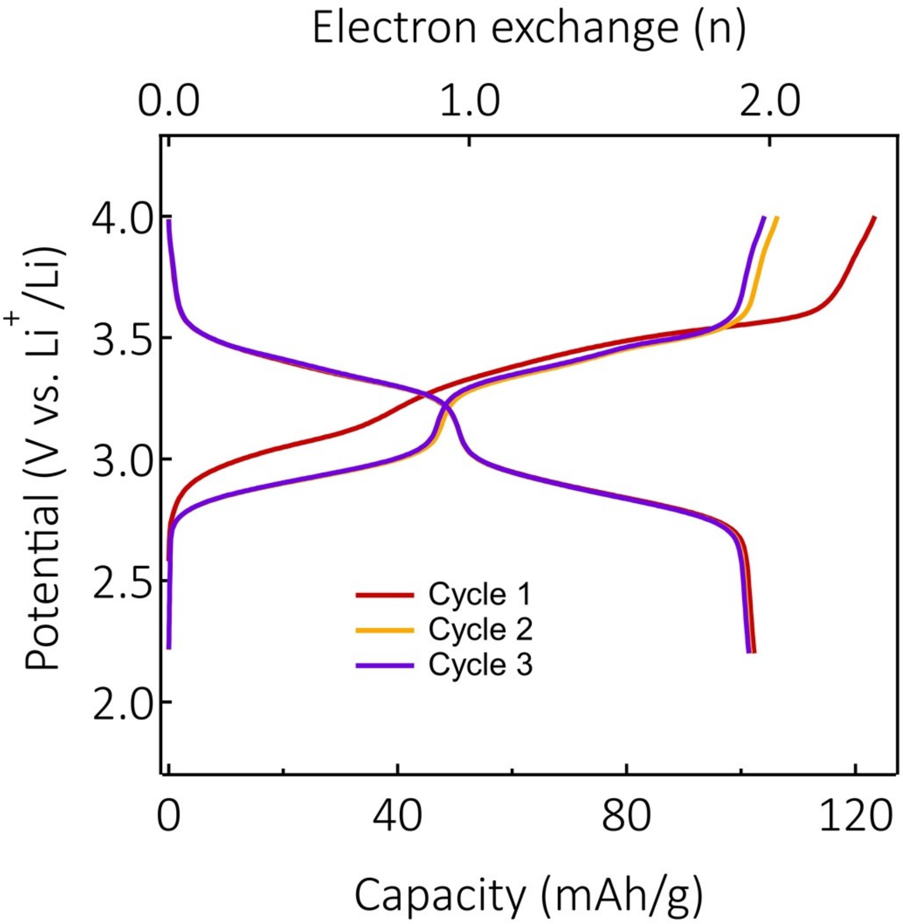

Figure S12. The first three cycles of Li$_2$-Co-PTtSA, cycled at a rate of C/5 (corresponding to one electron in 2.5 h). The compound can reversibly reach the two-electron theoretical capacity of 103 mAh/g.

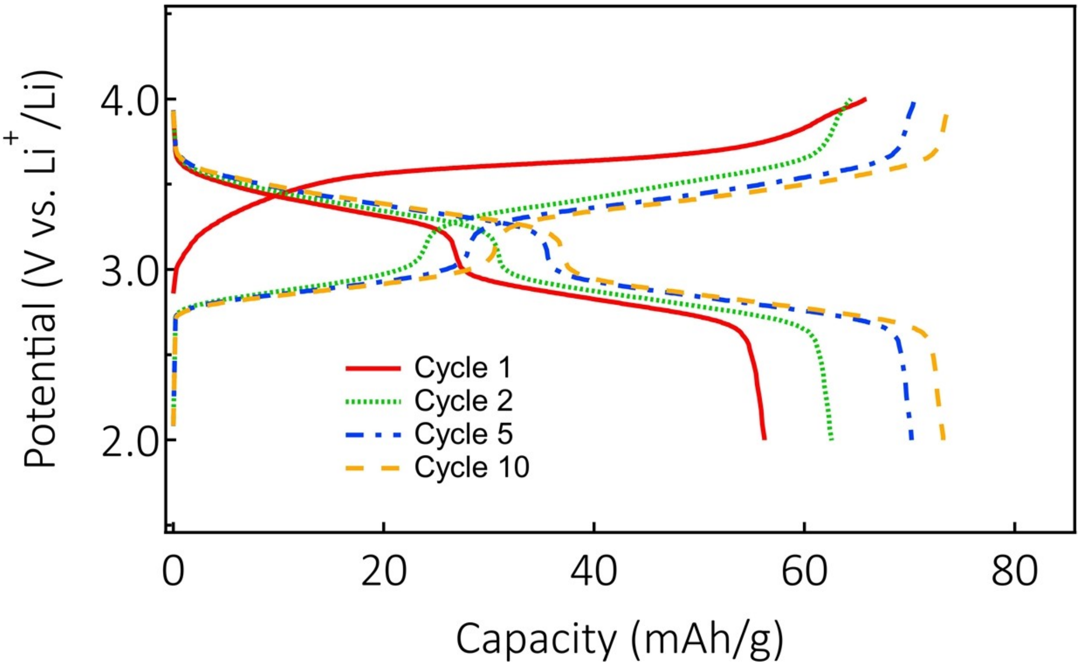

Figure S13. Charge-discharge curves of Li$_2$-Co-PTtSA electrode with 5% of Super P and 10% of PTFE. The electrode shows an activation process, with the capacity starting low in the first cycle and increasing steadily in the first 10 cycles, which could be due to under-optimized electrode formulation, inhomogeneous mixing of conductive carbon and electrode material, as well as particle size control.

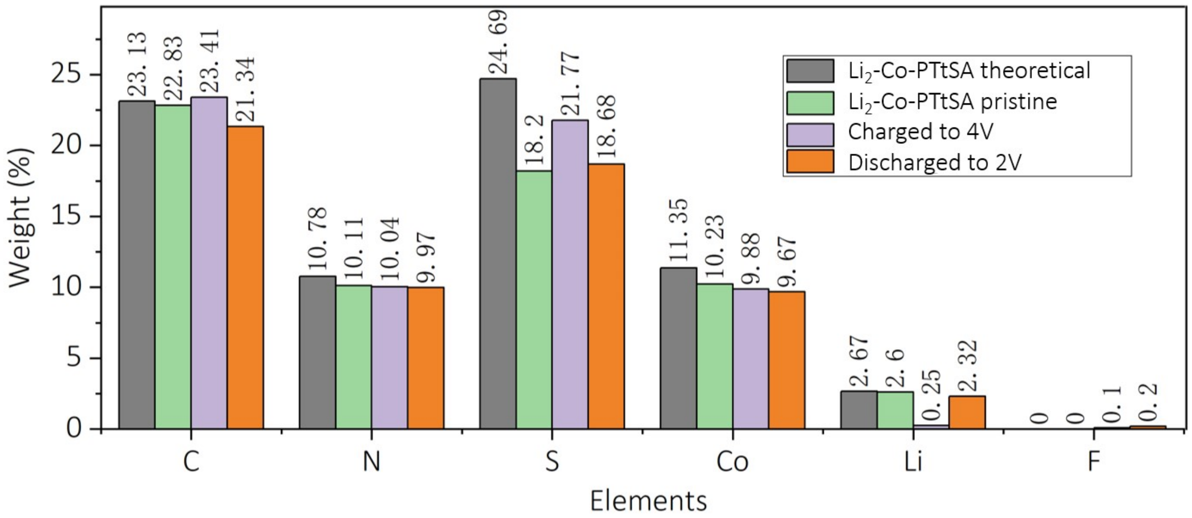

Figure S14. Ex-situ elemental analysis of Li$_2$-Co-PTtSA at three different charge states: pristine → charged to 4V → discharged to 2V. The content values of C, N and Co remain relatively constant (within the experimental error limit) during cycling. The S content fluctuations are due to higher measurement error, common for S determination using the CHNS/O technique. The essential feature is the loss of Li during charge and uptake of Li during discharge, which corroborates the redox mechanism of reversible two Li$^+$ exchange.

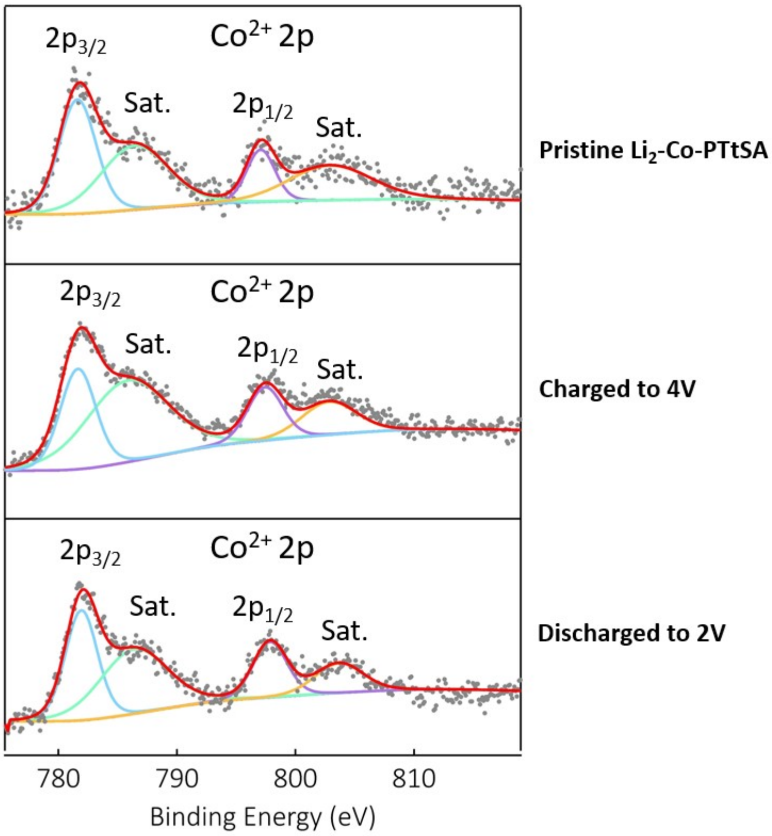

Figure S15. Ex-situ XPS analysis of Li_2-Co-PTtSA at three different charge states: pristine, charged (delithiated) to 4V and discharged (lithiated) to 2V. The analysis of Co^{2+} 2p results shows that the valence of cobalt is not changing during redox, confirming the two-electron reversible redox centered on the PTtSA ligand.

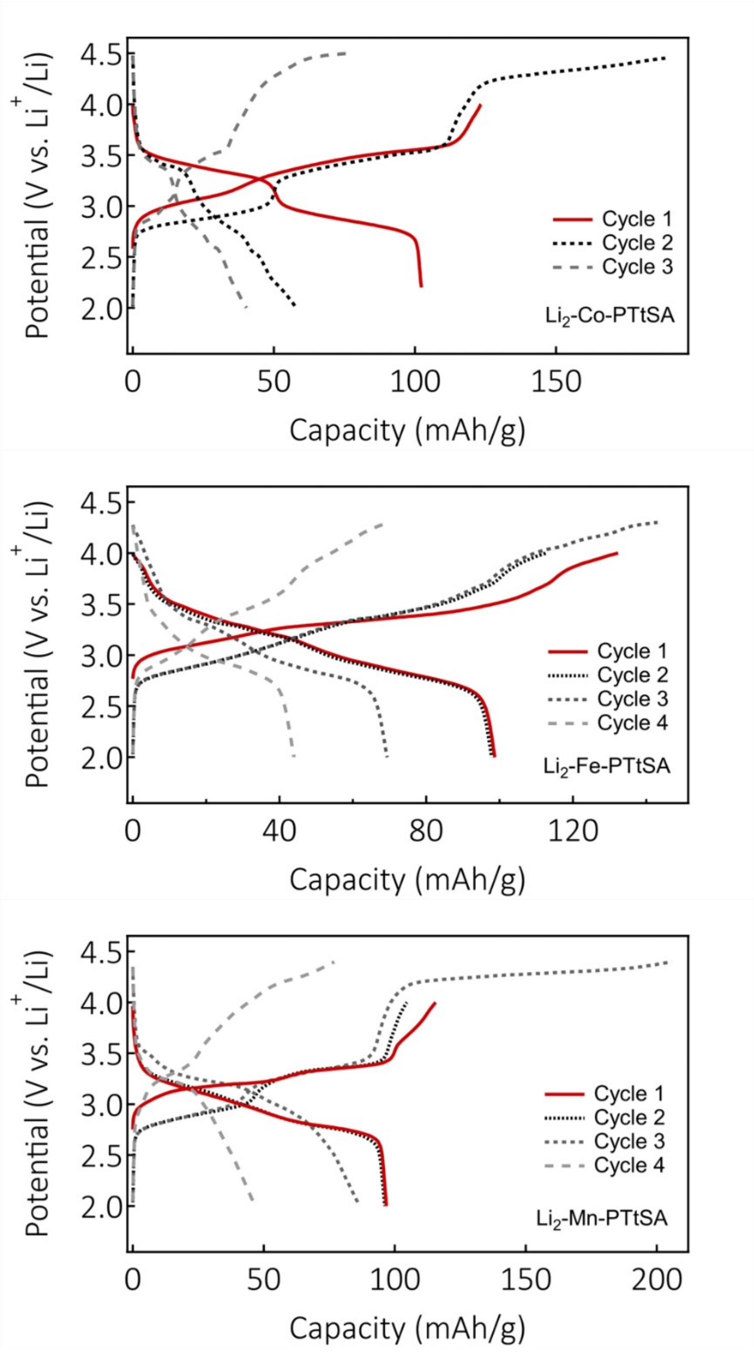

Figure S16. Potential-capacity profile plots of Li$_2$-TM-PTtSA (TM = Fe^{2+}, Co^{2+}, Mn^{2+}) electrodes cycled in the potential window of 2.0-4.0 V for two cycles, followed by extending the window to 2.0-4.5V for the next two cycles. This data shows that whereas higher charge capacity can be attained by going higher in potential (and accessing the redox of the TM center as well), the anion uptake within the CP host, as well as the instability of the coordination environment of the high-valence metal induces rapid and irreversible structural changes, material degradation and capacity loss.

DFT Calculation Section

1. Computational setup

The calculations were performed using SIESTA[2] which uses norm-conserving pseudopotentials and LCAO representation of the wavefunction. Periodic boundary conditions were imposed in order to simulate the infinite 1D chain of TM-PTtSA (TM=Co, Fe, Mn). The exchange correlation functional used was PBE for solid, PBEsol[3]; this choice is known to produce reliable geometric structures for molecular crystal bulk states[4].

Geometric models

The geometric structure of the atoms in the unit cell is represented in Figure S17. The chain was oriented along Z axis in a tetragonal cell with 65 Å size on OX and OY axes. The length of the cells along the OZ axis are summarized in Table S2 for all three systems. These values were obtained after structural relaxation of cell parameters and atomic positions up to gradients less than 0.01 eV/Ang.

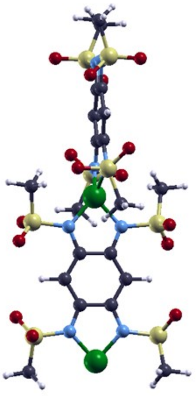

Figure S17: Geometric structure of the unit cell used in calculations; transition metal is represented in green. Each unit cell contains two PTtSA units with the pi-rings oriented perpendicular to each other. Periodic boundary conditions are applied to the system to form chains oriented along OZ axis; they are separated laterally by distances of 65 Å on OX and OY axes.

Table S2 : Unit cell length along OZ axis / average metal - nitrogen distances, in Angstrom, for the three M-PtTSA systems (M=Co, Fe, Mn), in the two oxidation states (Q is the total charge per unit cell; it corresponds to a charge q=-2 for each M-PTtSA unit in the chain).

	Co	Fe	Mn
Q=0	15.63 / 1.93	15.68 / 1.95	16.13 / 2.05
Q=-4	16.56 / 2.01	16.59 / 2.04	16.96 / 2.13

The main result to note here is that the length of the periodic cell along OZ as well as the metal-nitrogen distances are on inverse proportion to atomic numbers; this conclusion stands for both oxidation states. Also, we note that for charged systems this length is about 7 % longer in all cases, an indication of weaker bonding.

2. Results

2.1 Energy and spin

The values of the spin per unit cell (see Figure S17) are given in Table S3. We note the correlation between magnetic moments and the length of the unit cells in each case. Indeed, the large magnetic moments are correlated to large size of the periodic cell. In other words, magnetic moments are correlated with large volume occupied by the atom in 1D chain, which is explainable since spins with same orientation have the tendency to occupy larger volume. On the other hand, we note that the values of the magnetic moments are very close to those predicted by Hund's rule for isolated atoms: 3, 4 and 5 for Co, Fe and Mn, respectively. Moreover, by removing two electrons from each transition metal this rule is still valid.

Table S3 : Total spin of the three systems in the two oxidation states (charge per unit cell in periodic chain Q=0 / -4). Total value and value per transition metal atom (i.e. divided by two) are given.

	Co	Fe	Mn
Q=0	5.98/2.99	8.0/4.0	9.99/5.0
Q=-4	5.95/2.98	7.99/4.0	10.0/5.0

2.2 Density of states

Atom projected density of states for each TM-PTtSA system in the two oxidation states are summarized in Figures S18 – S20. Details for all atoms on a smaller scale were obtained by excluding from the plot the data for oxygen atoms (i.e. dominant contributions) and are given in Figures S21 - S23.

Common features for all systems: large contribution of the oxygen between -4 and -2 eV for neutral compound which is shifted about 1 eV downward for negatively charged systems. Small contributions from other atoms around Fermi level; the main are coming from transition metal and nitrogen atoms.

Differences: a gap at Fermi level is gradually enlarging from Co-PTtSA to Mn-PTtSA for both redox states. While for Co there seems to be no gap (i.e. a weak metallic character), for Fe-PTtSA a small gap is noticed for charged system, and a half-metallic character for the neutral state. Finally for the Mn-PTtSA, a gap around 0.2 eV is found in neutral state, while for the charged state the gap is close to 1 eV.

The orbitals of transition metals are gradually shifted for Co to Mn, so that for Co we have a maximum occupation of states at Fermi level, while for the Mn these states are empty. As a rule of thumb, this shift depends on each additional electron in the structure of transition metal. Let us note that the structure of the DOS explains partially the small deviations from Hund's rule seen in Table S2. Indeed, for Co a density of states at Fermi level leads to small changes of the electronic structure. On the other hand, for Mn and Fe the presence of a gap at Fermi level explains the integer number of spin-up / spin-down electrons in each case.

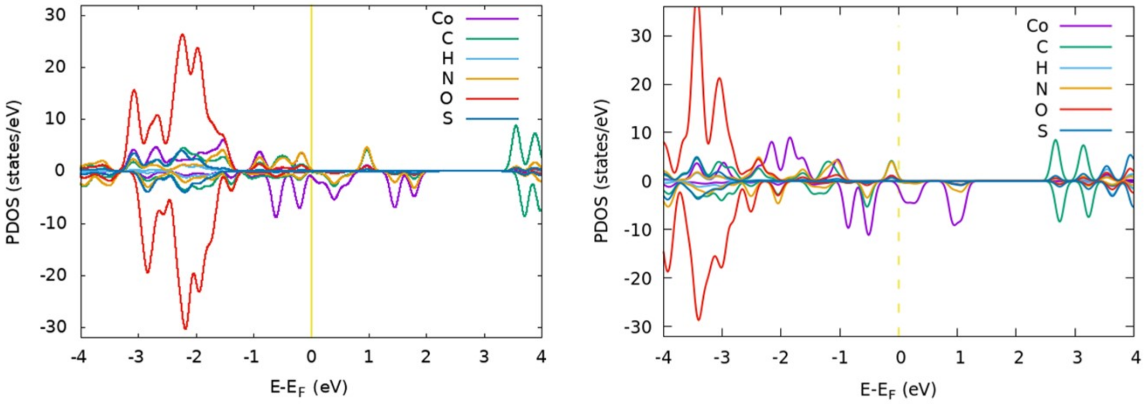

Figure S18 : Density of states for Co-PTtSA; left: charge Q=0; right: charge Q=-4.

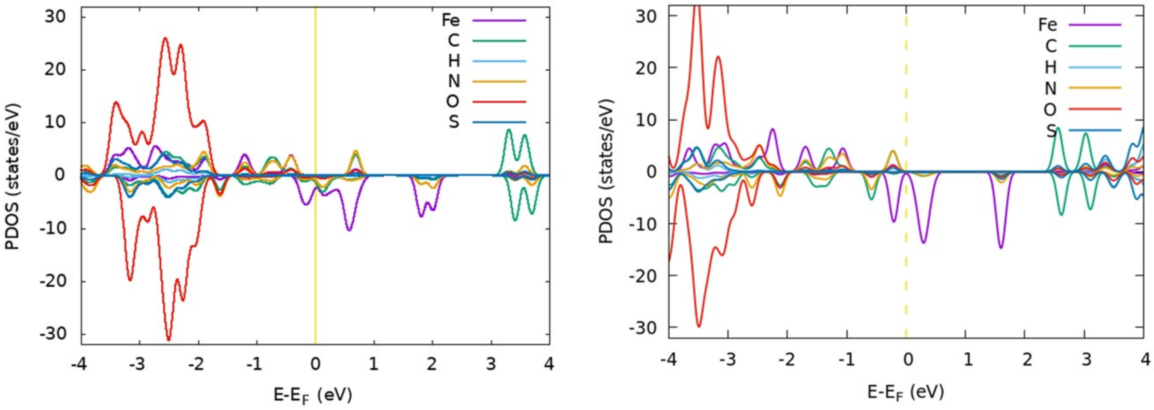

Figure S19 : Density of states for Fe-PTtSA**;** left: charge Q=0; right: charge Q=-4.

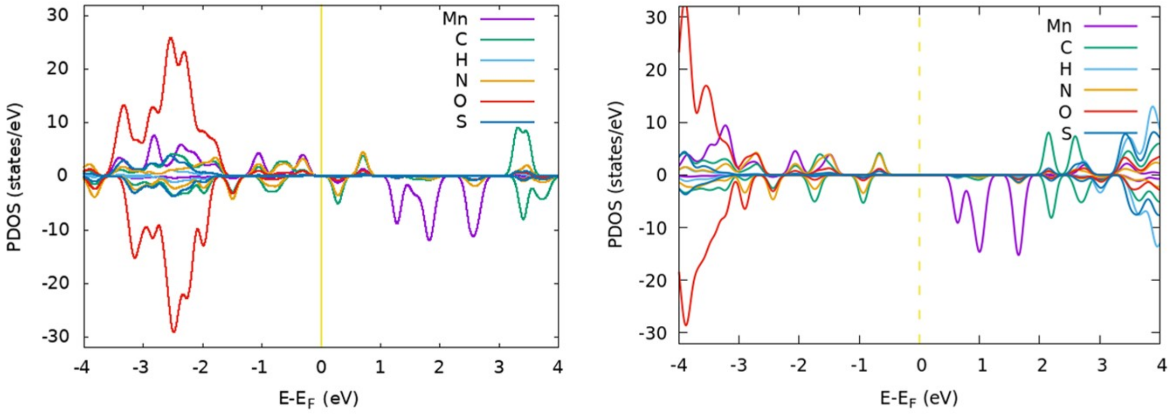

Figure S20: Density of states for Mn-PTtSA; left: charge Q=0; right: charge Q=-4.

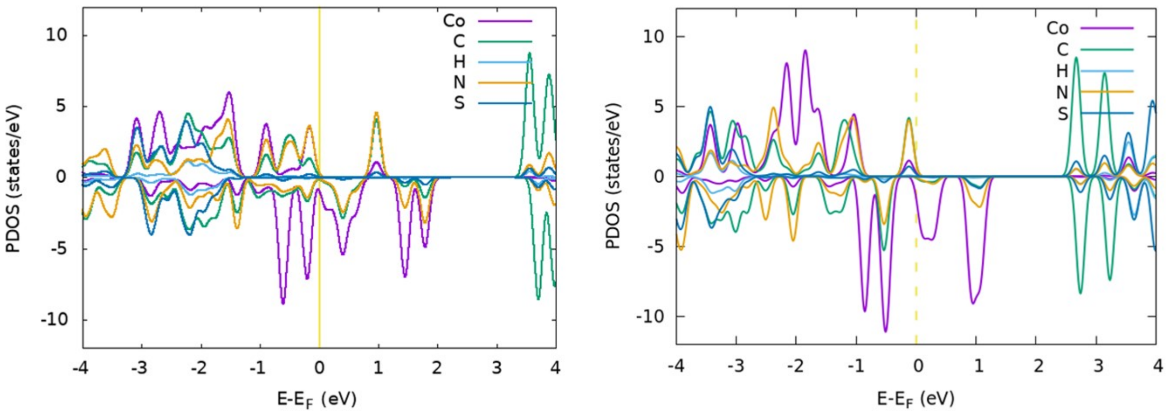

Figure S21: Details of density of states for Co-PTtSA; left: charge Q=0; right: charge Q=-4.

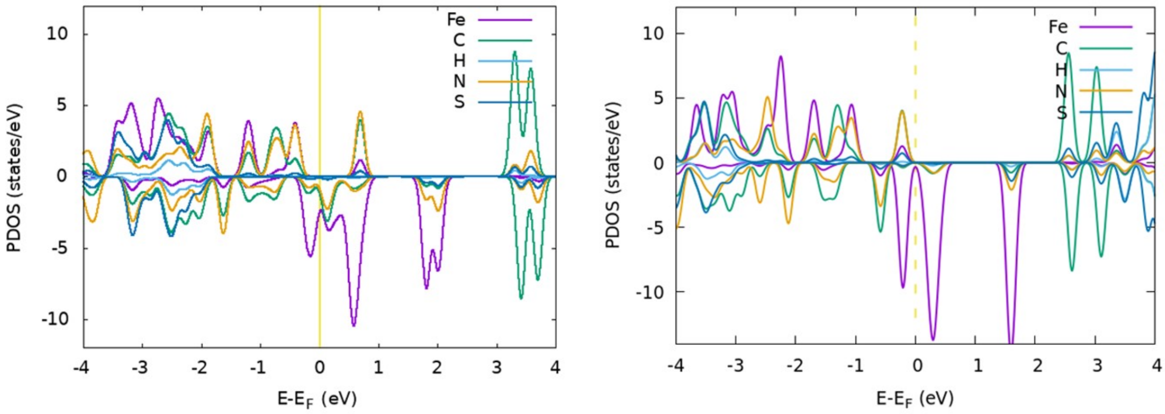

Figure S22 : Details of density of states for Fe-PTtSA**;** left: charge Q=0; right: charge Q=-4.

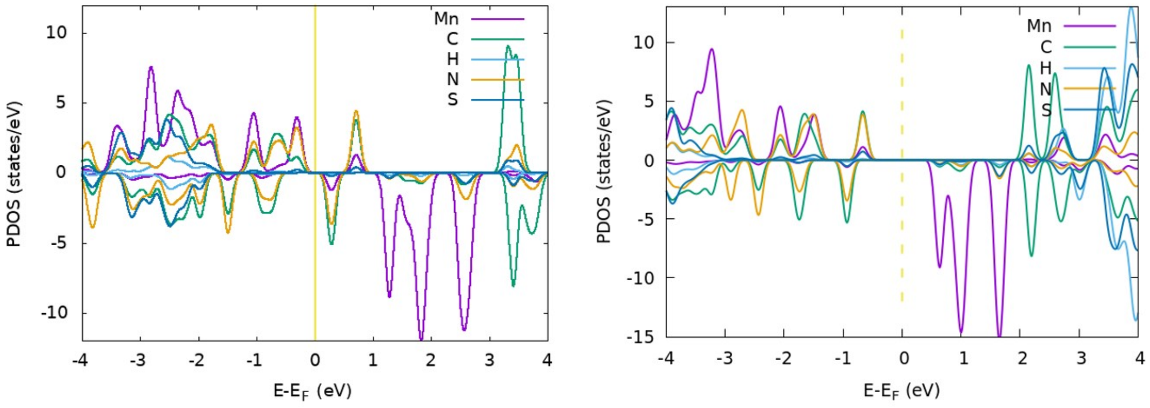

Figure S23 : Details of density of states for Mn-PtTSA; left: charge Q=0; right: charge Q=-4.

Projected density of states over 3d and 4s states for transition metal atoms (studied in this work) are presented in Figure S24. They show that the 4s states are located above Fermi level being responsible for the 2+ charge of each TM-PTtSA unit in the chain.

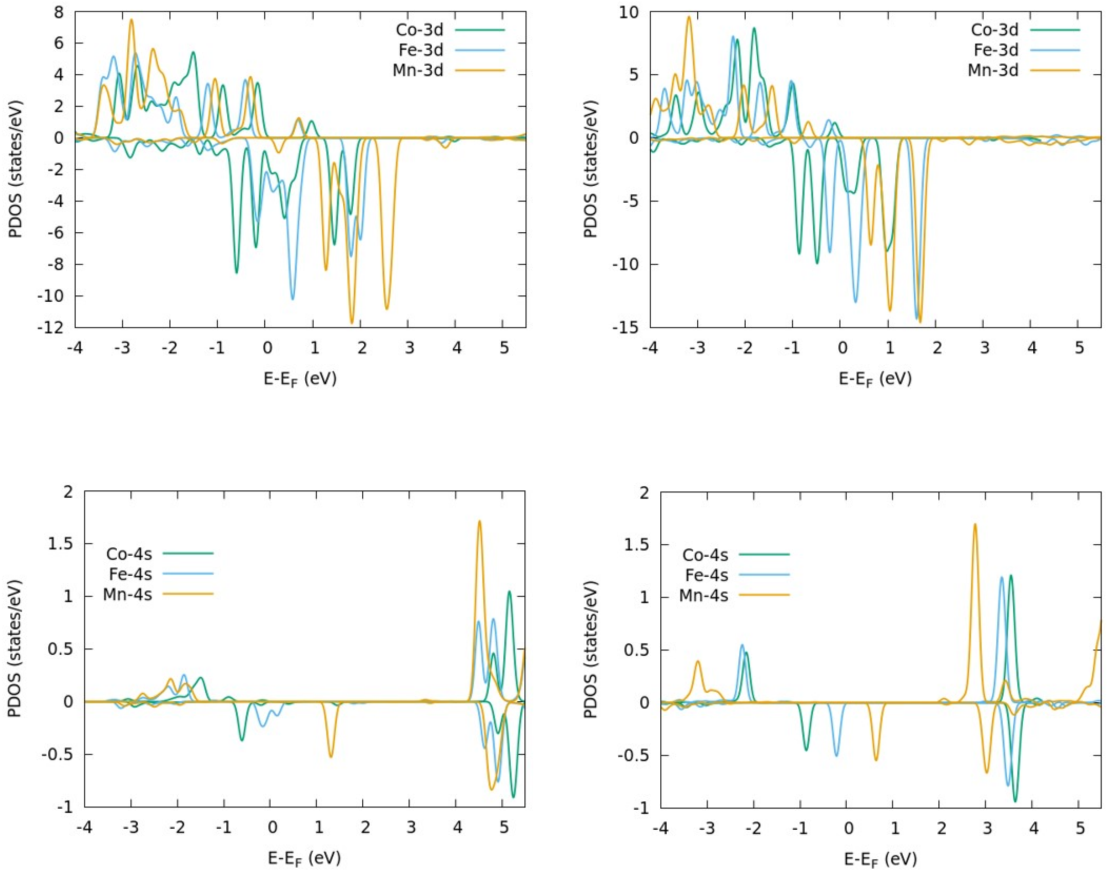

Figure S24: Density of states projected over 3d (top) and 4s (bottom) states of transition metals. Left: neutral system; right: charged systems (Q=-4 per unit cell / -2 per TM-PTtSA unit).

3. Conclusion

We calculate the geometric and electronic structure properties of 1D (chain) TM-PTtSA (TM = Co, Fe, Mn) using DFT and periodic boundary conditions. We found correlations between the values of the spin and the geometric properties: higher spin states correspond to larger unit cells for the 1D chain. Moreover, spin moments of all transition metal atoms in the chain are fully consistent with Hund’s rule for single atoms in both oxidation states. Atom-projected density of states reveal a large contribution of oxygen atoms at -2 to -4 eV below Fermi level. Contributions of other atoms are less than 20%, compared to oxygen. At Fermi level the DOS is relatively small; most are contributions of nitrogen and transition metal. The DOS of 3D orbitals of TMs follows a homogeneous trend, with a gap gradually opened form Co to Mn. While for Co-PTtSA there is no gap at Fermi level, for Fe-PTtSA we note a very small gap only for charged system while for Mn-PtTSA the gap has largest values, for both states (of 0.2 and 1 eV for the two oxidation states).

Reference, SI Section

1. Jiande Wang, Xuelian Liu, He Jia, Petru Apostol, Xiaolong Guo, Fabio Lucaccioni, Xiaozhe Zhang, Qi Zhu, Cristian Morari, Jean-François Gohy, and Alexandru Vlad, ACS Energy Letters (accepted) DOI: 10.1021/acsenergylett.1c02571

1. a) Ordejón, P.; Artacho, E.; Soler, J. M. Self-Consistent Order-N Density-Functional Calculations for Very Large Systems. Phys. Rev. B: Condens. Matter Mater. Phys. 1996, 118, R10441−R10444. b) Soler, J. M.; Artacho, E.; Gale, J. D.; García, A.; Junquera, J.; Ordejón, P.; Sánchez-Portal, D. The SIESTA Method for Ab Initio Order-N Materials Simulation. *J. Phys.: Condens. Matter* 2002, 14, 2745−2779.

2. J. P. Perdew et al, Phys. Rev. Lett. 100, 136406 (2008)

3. J. Quertinmont, A. Carletta, N. A. Tumanov, T. Leyssens, J. Wouters, and B. Champagne, "Assessing Density Functional Theory Approaches for Predicting the Structure and Relative Energy of Salicylideneaniline Molecular Switches in the Solid State" J. Phys. Chem. C 2017, 121, 6898−6908.

4. S. Renault , S. Gottis , A.-L. Barrès , M. Courty , O. Chauvet , F. Dolhem and P. Poizot , Energy Environ. Sci., 2013, 6 , 2124 —2133

5. Shiwen Wang, Lijiang Wang, Kai Zhang, Zhiqiang Zhu, Zhanliang Tao, and Jun Chen, Nano Letters 2013 13 (9), 4404-4409

6. L. Sieuw, A. E. Lakraychi, D. Rambabu, K. Robeyns, A. Jouhara, G. Borodi, C. Morari, P. Poizot and A. Vlad, Chemistry of Materials, 2020, 32, 9996-10006.

7. Lakraychi, A. E.; Deunf, E.; Fahsi, K.; Jimenez, P.; Bonnet, J. P.; Djedaini-Pilard, F.; Bécuwe, M.; Poizot, P.; Dolhem, F. An air-stable lithiated cathode material based on a 1,4-benzenedisulfonate backbone for organic Li-ion batteries. Journal of Materials Chemistry A 2018, 6 (39), 19182– 19189

8. A. Jouhara, N. Dupré, A.-C. Gaillot, D. Guyomard, F. Dolhem and P. Poizot, Nature Communications, 2018, 9, 4401.

9. D. Rambabu, A. E. Lakraychi, J. Wang, L. Sieuw, D. Gupta, P. Apostol, G. Chanteux, T. Goossens, K. Robeyns and A. Vlad, Journal of the American Chemical Society, 2021, 143, 11641-11650.

10. J. Wang, A. E. Lakraychi, X. Liu, L. Sieuw, C. Morari, P. Poizot and A. Vlad, Nature Materials, 2021, 20, 665-673.

11. Wang, S., Wang, L., Zhu, Z., Hu, Z., Zhao, Q. and Chen, J. (2014), All Organic Sodium-Ion Batteries with $Na_4C_8H_2O_6$. Angew. Chem. Int. Ed., 53: 5892-5896

12. J. Wang, X. Liu, H. Jia, P. Apostol, X. Guo, F. Lucaccioni, X. Zhang, Q. Zhu, C. Morari, J.-F. Gohy and A. Vlad, ACS Energy Letters, 2022, DOI: 10.1021/acsenergylett.1c02571, 668-674.